RSC Advances

PAPER

View Article Online
View Journal | View Issue

Cite this: *RSC Adv.*, 2026, **16**, 18359

A multi-stage computational pipeline and *in vitro* validation for the discovery of small-molecule translation inhibitors targeting the bacterial ribosome

Merve Yuce, †[a] Ezgi Koman, †[bc] Fethiye Aylin Sungur, [d] Ayten Yazgan-Karatas [bc] and Ozge Kurkcuoglu *[a]

The global rise in antibiotic resistance necessitates new agents targeting essential bacterial processes like protein synthesis. Structure-based virtual screening enables the rapid identification of drug candidates from large chemical libraries, accelerating drug discovery. Here, we report an integrated computational and experimental pipeline to identify small-molecule translation inhibitors targeting the catalytic cavity of the *E. coli* ribosome. A consensus docking strategy using Glide and AutoDock Vina, combined with pharmacophore filtering and interaction analysis, was applied to FDA-approved, experimental, and investigational drug libraries to prioritize candidate compounds. The binding free energies of the compounds were estimated using restrained molecular dynamics (MD) simulations coupled with the MM-GBSA method, where the computational efficiency was improved by truncating the ribosome-ligand complexes. Guided by these results and our previous work on the *E. coli* 30S decoding center, 14 hit compounds were selected for the *in vitro* antibacterial and translation inhibition assays. Among these, Mitoxantrone (IC_{50} = 14.10 ± 0.38 μM) was identified as a translation inhibitor with a bacteriostatic effect comparable to the antibiotic Clindamycin. Whereas Plerixafor (IC_{50} = 62.30 ± 6.47 μM), Olcegepant (IC_{50} = 144.30 ± 16.41 μM), and Ziritaxestat (IC_{50} = 224.30 ± 25.02 μM) showed inhibitory effects at higher concentrations. Notably, Mitoxantrone has the potential to be an anticancer agent and a translation inhibitor that may significantly benefit cancer patients by addressing secondary bacterial infections. The pharmacokinetic and toxicological profiles of these compounds are already well-characterized. Overall, this work illustrates a useful drug discovery strategy combining virtual screening, MD simulations, and experimental validation to identify ribosome-targeting inhibitors and can be extended to other challenging RNA targets and protein-RNA complexes.

Received 2nd March 2026
Accepted 30th March 2026

DOI: 10.1039/d6ra01785a

rsc.li/rsc-advances

Introduction

A major concern for public health around the world is the alarming rise in pathogens that are resistant to antibiotics, which makes it harder to treat infections that were previously curable. Antibiotic-resistant bacterial infections are getting progressively more challenging to manage, leading to higher healthcare costs, longer hospital stays, and increased mortality rates.[1] The major target for antibiotic therapy is the bacterial ribosome, the molecular machine responsible for the translation of the genetic information into functional proteins in living cells. The bacterial ribosome is a supramolecule that consists of a small subunit (30S) and a large subunit (50S), including ribosomal RNAs (rRNAs) along with ~50 ribosomal proteins. Numerous functional sites, such as the peptidyl transferase center (PTC) on the 50S large subunit, are targeted by diverse classes of antibiotics that inhibit protein synthesis, thereby suppressing bacterial growth.[2–4] Current drug development strategies focus on structural modifications of conventional antibiotics to overcome the antibiotic resistance problem, such as the macrobicyclic Cresomycin derived from lincosamides,[5] antimicrobial peptides Api137, Api88 derivative of honeybee PrAMP Apidaecin,[6] synthetic macrolides MCX-219 and MCX-190,[7] and macrobicyclic antibiotic BT-33.[8] Due to the increasing problem of antibiotic resistance, identifying new compounds with different mechanisms to inhibit protein translation is essential to treat bacterial infections.

[a]*Istanbul Technical University, Department of Chemical Engineering, Istanbul 34469, Turkey. E-mail: olevitas@itu.edu.tr; merveyuce@itu.edu.tr*

[b]*Istanbul Technical University, Department of Molecular Biology and Genetics, Istanbul 34469, Turkey. E-mail: koman@itu.edu.tr; karatasay@itu.edu.tr*

[c]*Istanbul Technical University, Molecular Biology-Biotechnology and Genetics Research Center (MOBGAM), Istanbul 34469, Turkey*

[d]*Istanbul Technical University, Computational Science and Engineering Division, Informatics Institute, Istanbul 34469, Turkey. E-mail: aylin.sungur@itu.edu.tr*

† These authors contributed equally.

Structure-based drug design, utilizing virtual screening of diverse compound libraries against targets with known three-dimensional structures, has emerged as a powerful strategy in drug discovery. Molecular docking has a notable benefit in efficiently identifying new chemotypes from an enormous chemical library for the target region,[9] potentially leading to new biological effects compared to known ligands.[9] On the other hand, the discovery of successful therapies can be accelerated by drug repurposing (or repositioning), thus avoiding the time-consuming and expensive process of developing new drugs from scratch.[10] The repurposed drugs may possess high toxicity, possibly due to their dosages or their routes of administration. However, their toxicity profiles may be different for the new application that can be revealed after a careful evaluation. While these approaches are well-established for proteins, their development and adaptation for RNA molecules are still in progress.[11] Compared to proteins, RNA structures are challenging targets due to their intrinsic structural flexibility, high electronegativity, and poorly understood structure–function relationships.[12] Nonetheless, with the increasing number of 3-dimensional structures of RNA systems available in the protein data bank (https://www.rcsb.org/), computational studies such as molecular docking and molecular dynamics (MD) simulations have provided valuable insights for developing novel RNA-targeted therapeutics.[12] Early computational efforts focused on optimizing parameters in software such as AutoDock (v3.0),[13] DOCK (v3.5.54),[14] GOLD (v4.0),[15] and Glide (v5.0)[15] to improve the accuracy of predicting the crystal poses of ligands in RNA cavities. Gradually, the growing repository of biochemical and structural data has provided valuable insights into the structural characteristics of RNA binding sites while stimulating the development of RNA-specific scoring functions[16–19] and RNA-focused docking software, such as rDock,[20] the fragment-based approach SILCS-RNA,[21] and the meta-dynamics enhanced-sampling method SHAMAN.[22] Furthermore, artificial intelligence-based virtual screening tools, such as FingeRNAt,[23] Rlaffinity,[24] and RNAmigos2,[25] have been introduced to accelerate RNA-targeted drug discovery. Despite these advancements, the rational design of novel and effective compounds to target the bacterial ribosome remains uncharted, mostly due to its 2.5 MDa size.

In this study, we targeted the PTC of the bacterial ribosome, a highly conserved ribosomal RNA (rRNA) cavity responsible for catalyzing peptide bond formation between the amino acids attached to CCA ends of the A- and P-transfer RNA (tRNA) recruited to the complex.[26] The binding sites of conventional antibiotics targeting PTC are either at the A-site (such as Chloramphenicol, lincosamides like Clindamycin, oxazolidinones like Linezolid, Puromycin, and Sparsomycin) or the P-site (Blasticidin S), or they span both the A- and P-sites (such as the pleuromutilin and streptogramin A class).[27] We implemented an integrated virtual screening pipeline to identify high-affinity ligands from FDA-approved, investigational, and experimental drug libraries against the PTC cavity of *E. coli* ribosome. To enhance the reliability of our predictions, we employed a consensus docking strategy using Glide[28] and AutoDock Vina 1.1.2,[29] where the convergence of diverse scoring functions represents an effective strategy for enhancing the success rate in identifying plausible hits.[30] The resulting candidates were further filtered using a pharmacophore model derived from the binding modes of the known PTC-targeting antibiotics. The binding poses of the selected hits were subsequently assessed with the all-atom MD simulations, and the effective binding energies of the hits were estimated using the Molecular Mechanics with Generalized Born Surface Area (MM-GBSA) method. To ensure computational efficiency, a truncated 50S subunit model was utilized, with harmonic restraints applied to the outermost residues to maintain structural integrity, similar to previous studies.[31–33] Based on the results of our earlier study on the decoding center of *E. coli* 30S small subunit,[34] and the current research focusing on the *E. coli* 50S large subunit, the hit compounds were selected for further testing with *in vitro* experiments. *In vitro* assays identified one inhibitor and three lead compounds, offering new scaffolds for combating antibiotic resistance while also paving the way for the rational design of the next-generation antibiotics. To the best of our knowledge, this is the first study to combine large-scale virtual screening, drug repurposing, and *in vitro* evaluation specifically for the bacterial PTC, providing a clear and reproducible procedure for future drug discovery efforts on challenging macromolecular systems in medicinal chemistry.

Materials and methods

We employed a computational and experimental workflow to identify novel inhibitors targeting the Peptidyl Transferase Center (PTC) of the *E. coli* 50S ribosomal subunit. Virtual screening was initiated using FDA-approved, experimental, and investigational compound libraries. Two molecular docking programs, Glide and AutoDock Vina 1.1.2, were utilized to generate and evaluate binding poses, with hit selection based on the consensus of their distinct scoring functions. A PTC-specific pharmacophore model was derived from 12 nucleotides predominantly involved in key interactions with PTC-targeting antibiotics, and docked compounds satisfying this pharmacophore hypothesis were retained for further evaluation. The stability and suitability of the predicted binding modes were assessed through independent all-atom molecular dynamics (MD) simulations performed in Desmond. Subsequently, compounds representing diverse chemotypes were subjected to a series of experimental assays, including minimum inhibitory concentration (MIC), minimum bactericidal concentration (MBC), time-kill kinetics, and *in vitro* translation inhibition assays to identify functional inhibitors of the *E. coli* ribosome.

Molecular docking calculations

Dataset preparation. A total of 12 449 compounds in SDF format were initially retrieved from the DrugBank database[35] and prepared using the LigPrep module (Schrödinger Release 2021-4, Schrödinger, LLC, New York, NY, USA). As individual molecules in DrugBank may be listed under multiple categories, a deduplication step was implemented to eliminate the

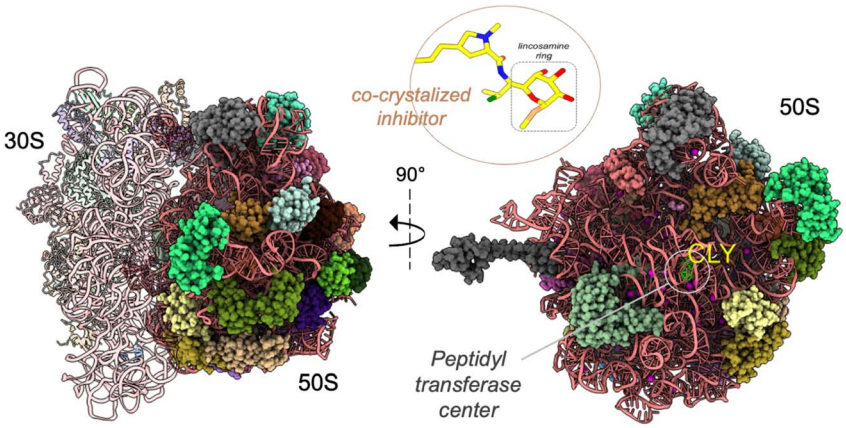

Fig. 1 Cartoon representation of *E. coli* 70S ribosome (PDB ID 4v7v), where small (30S) and large (50S) subunits are displayed with ribosomal proteins on the left. The investigated region, including the peptidyl transferase center on 23S rRNA, is indicated on 50S on the right. The native inhibitor Clindamycin (CLY) is shown in sticks. Mg^{2+} ions in the crystal structure are depicted as magenta spheres.

overlapping entries across categories. This ensured that each unique compound was represented only once in the dataset. After the removal of the overlapping entries, a total of 10 885 unique compounds, including 2481 FDA-approved compounds, 5955 experimental compounds, and 2449 investigational compounds, was subsequently used in the ligand preparation step. Ligand preparation included energy minimization with the OPLS-2005 force field[35] and ionization state assignment at pH 7.0 ± 0.5 using the Epik ionization tool (Schrödinger Release 2021-4) to reflect physiological conditions. Multiple conformations were generated for each compound, and the lowest energy conformations were selected for the molecular docking calculations. Prepared structures were saved in MAE and PDB formats.

The *E. coli* 50S ribosomal large subunit (PDB ID: 4v7v) in complex with Clindamycin[36] (Fig. 1) was prepared using the Protein Preparation Wizard (Schrödinger Release 2021-4). During receptor preparation, crystallographic water molecules were treated selectively. Only three water molecules located within 5 Å of the co-crystallized ligand Clindamycin were kept, as these are positioned to potentially mediate ligand–receptor interactions. Mg^{2+} ions were maintained in the structure, whereas all ribosomal proteins were removed since none were close to the docking site. Missing hydrogen and side chain atoms were added with the Protein Preparation Wizard module. PROPKA was employed to adjust the protonation states of amino acids, while Epik was utilized to predict the ionization and tautomeric states of the co-crystallized ligand under the physiological pH of 7.0. Subsequently, the 50S large subunit was subjected to energy minimization under the OPLS-2005 force field to eliminate steric overlaps resulting from the addition of hydrogens to the structure. Energy minimization was carried out using the Impref module,[37] where the root mean squared deviation (RMSD) tolerance for heavy atoms was set to 0.3 Å. The final prepared 50S ribosomal large subunit consisted of approximately 98 000 atoms.

Molecular docking. Two molecular docking programs, Glide[28,38] and AutoDock Vina 1.1.2,[29] were employed to enable consensus of two different scoring functions and improve hit reliability. In Glide, the Receptor Grid Generation module (Schrodinger Release 2021-4) was used to determine the grid box size and the center of the grid box using the native ligand, which was *x*: 75.7 Å, *y*: −57.1 Å, and *z*: 1.5 Å. The outer grid box was sized as 30.0 × 30.0 × 30.0 $Å^3$ while the inner grid box was 10.0 × 10.0 × 10.0 $Å^3$. During the docking calculations performed with the OPLS-2005 force field,[39] the dihedral angles of the compounds were kept flexible while the receptor (including 23S and 5S rRNA, crystal waters, and crystal Mg^{2+} ions) was kept rigid. Docking calculations performed in the default docking mode, SP-docking (standard precision),[28] were continued in the XP-docking (extra precision) mode.[38] The XP scoring function (XP GlideScore) includes additional terms over the SP scoring function to improve sampling and reduce the number of false positives, following a sampling approach based on the anchor and refined grow strategy. Accordingly, anchor fragments of the docked ligand (typically rings) are taken from the SP-docking poses. The molecule is regrown using this anchor while the growing is focused on attempting to relieve any XP scoring penalties and to optimize the best scoring poses.

In AutoDock-Vina 1.1.2,[29] docking cannot be performed with water molecules; thus, crystal waters were removed from the prepared 50S structure. The receptor was then prepared using the AutoDock-Tools (1.5.7) interface. The chelate Mg^{2+} ions were parameterized with AutoDock-Tools, and after the receptor preparation, the cation charges were manually set to +2. The pdbqt files of the compounds were prepared using the Python script prepare_ligand4.py. The center of the grid box was determined as $x = -75.212$ Å, $y = -57.534$ Å, and $z = 1.456$ Å with the dimensions of 25 × 25 × 25 $Å^3$. An exhaustiveness value of 32 was chosen, where higher exhaustiveness values yield a significant improvement and a successful reproduction for docking.[40] The empirical and knowledge-based scoring function of AutoDock-Vina calculates the binding affinity and ranks the binding orientations, which is the sum of the contribution of each weighted energetic factor.[29] The Vina scoring function consists of the sum of the weights of the steric

interactions (attractive Gaussian and Repulsion terms), hydrophobic interactions, and the hydrogen bonding interactions between the atoms. More information on the molecular docking calculations is provided in the SI file.

Prime MM-GBSA calculations. Prime MM-GBSA calculations estimated the binding energy (Prime MM-GBSA, kcal mol^{-1}) based on ligand docking poses in the binding site using the Prime module. The VSGB 2.0 (variable-dielectric generalized Born) solvent model[41] and OPLS-2005 force field were employed. The Generalized Born Surface model, derived from the variable dielectric approximation and Poisson–Boltzmann equation, forms the basis of this implicit solvent model. The Prime MM-GBSA method calculates the ligand, receptor, and ligand-receptor energies of the molecules generated by docking using the following equation:

$$\Delta G_{\text{bind,Prime}} = E_{\text{complex(minimized)}} - (E_{\text{ligand(minimized)}} + E_{\text{receptor(minimized)}}) \quad (1)$$

In this equation, each E term contains both $E_{\text{electrostatic}}$ ($E_{\text{Coulomb}} + H_{\text{bond}} + E_{\text{GB}}$) and E_{vDW} ($E_{\text{vDW}} + E_{\pi-\pi} + E_{\text{self-contact}}$) terms. Worth noting that the Prime MM-GBSA scoring function may yield more negative values than actual binding energy values. The maximum number of atoms allowed by the Prime module of Schrödinger prevented the usage of the intact 50S large subunit. Here, a truncated ribosomal structure with a radius of 40 Å was constructed by centering Clindamycin, similar to previous studies with small molecules[31–33,42] as well as peptide drugs.[6] Ions (Mg^{2+}) and water molecules were removed from the prepared truncated structure during the Prime MM-GBSA calculations.

Pharmacophore design and phase screening. Hit compounds from Glide and AutoDock-Vina calculations were further filtered using a pharmacophore model. For the pharmacophore model, the Phase module of the Maestro program was used (Schrödinger Release 2021-4). In the Develop Pharmacophore Hypothesis panel of the Phase module, 12 nucleotides (A2058, A2059, G2061, A2062, A2451, C2452, A2503, U2504, G2505, U2506, G2583, and U2585) that are noted to mostly interact with the PTC-binding antibiotics were defined (Fig. S1) and their features were identified. In pharmacophore design, fragments with properties were placed instead of a single ligand, and common features that meet criteria regarding their location and orientation were selected. The pharmacophore model was created by including a maximum of 8 features with the best scores based on Glide XP scoring terms for the fragments inserted into the receptor (e-pharmacophore model). The Phase module of the Schrödinger suite provides six distinct pharmacophore features: hydrogen bond acceptor (A), hydrogen bond donor (D), hydrophobic group (H), negatively charged group (N), positively charged group (P), and aromatic ring (R). The pharmacophore model developed in this study consisted of the following features: hydrophobic (H18), aromatic ring (R24, R26, R28), hydrogen bond acceptor (A1, A8), and hydrogen bond donor (D11, D12) (Fig. S2). The Phase Ligand Screening tool was employed to filter hit compounds that matched the generated pharmacophore hypothesis.

Molecular dynamics simulations

All-atom molecular dynamics (MD) simulations in explicit water were employed to assess the docking poses of the compounds at the binding sites and analyze their interactions with specific nucleic acid or amino acid residues. The 50S large subunit contains more than 90 000 atoms, and it is computationally inefficient to study the entire structure with MD simulations using an explicit solvent model at the atomic level. To maintain computational efficiency, the MD simulations were performed for a spherical region truncated from the bacterial ribosome, centering the docking site. Therefore, only the fluctuations and interactions at the binding site were analyzed, and the global motions that may occur due to drug binding were not investigated.

System preparation. The *E. coli* ribosome (PDB ID: 4v7v) in complex with the antibiotic Clindamycin was used to test the truncated structure in the MD simulations. A spherical region with a 40 Å radius centering the lincosamide antibiotic Clindamycin binding site was truncated from the 50S, including the rRNA and ribosomal proteins (Fig. S3(a)), similar to a previous study.[33] The 40 Å cutoff was considered a relatively large distance to include the electrostatic interactions between the ligand and the ribosome. The missing nucleotides on the 23S rRNA and ribosomal protein chains were completed, and chains shorter than 5 nucleotides were deleted to form a truncated globular region. Mg^{2+} ions and crystal waters were preserved in the truncated region. The resulting truncated structure contained 23S rRNA (728 nucleotides), ribosomal proteins L2 (23 residues), L3 (53 residues), L4 (37 residues), L13 (11 residues), L14 (9 residues), L15 (35 residues), L16 (19 residues), L20 (36 residues), L21 (9 residues), L22 (23 residues), L32 (19 residues), and L34 (8 residues), 71 Mg^{2+} ions and 333 crystal water molecules. Truncated ribosomal structure in complex with the docked compounds was prepared in Protein Preparation Wizard in Maestro (Schrödinger Release 2021-4), and the charge of the compound was assigned. The prepared truncated structure consisted of approximately 29 200 atoms and had a net charge of −538 (excluding ligand).

The Desmond package with the OPLS-2005 force field[39] was used in the MD simulations.[43] The simulation system was prepared using Desmond's System Builder module (Schrödinger Release 2021-4). TIP3P solvent model and a cubic water box with a buffer distance of 15 Å were used. K^+ ions sufficient to neutralize the charge of the system were added, and KCl salt was introduced to set the ionic strength to 0.15 M to mimic the physiological conditions. The prepared system contained ~211 000 atoms, including 23S rRNA, ribosomal proteins, ligand, solvent, and ions (Mg^{2+}, K^+, and Cl^-).

Simulation protocol. MD simulations consisted of 3 steps: energy minimization, relaxation, and production. Using Desmond's Minimization module, the prepared system was minimized for 100 ps with the OPLS-2005 force field.[39] During energy minimization, a harmonic restraint of 50 kcal mol^{-1} $Å^{-2}$ was applied to solute atoms using a hybrid method of the steepest descent and the limited memory Broyden-Fletcher-Goldfarb-Shanno algorithms implemented in the module to remove the

steric clashes. The relaxation protocol of Desmond was employed to equilibrate the system. First, a simulation of 100 ps was conducted with the NVT ensemble at 10 K using Brownian dynamics. Then, a 12 ps long simulation was performed using the Langevin thermostat at 10 K in the NVT ensemble. For the third stage, the Langevin thermostat and the Langevin barostat were used at 10 K and 1 atm in the NPT ensemble for 12 ps. In the fourth step, the temperature increased to 300 K under the same conditions. In the first four steps of the relaxation protocol, a harmonic constraint of 50 kcal mol^{-1} $Å^{-2}$ was applied to all heavy atoms in the structure, including the chelate Mg^{2+} ions. At the last step, a 24 ps simulation was performed using the same parameters except for the restraints. To prevent structural collapse of the truncated model, the system was divided into three concentric zones based on distance from the ligand (Fig. S3(b)):

- Innermost zone (≤24 Å): fully flexible, including the binding site, ligand, and coordinating nucleotides and Mg^{2+} ions.
- Middle zone (24–32 Å): restrained with a harmonic restraint of 25 kcal mol^{-1} $Å^{-2}$
- Outermost zone (>32 Å): restrained with a harmonic restraint of 50 kcal mol^{-1} $Å^{-2}$

The production runs were performed for 100 ns in three replicas for the same initial structures using different velocity distributions. Langevin thermostat and a Langevin barostat in the NPT ensemble were used to set the temperature and the pressure at 310 K and 1.013 bar, respectively. A 12 Å cutoff radius was set for the short-range electrostatic interactions. The long-range interactions were estimated using the Particle Mesh Ewald (PME) method.[44] A time step of 2 fs was used. The harmonic restraints for the middle and outermost zones were also applied during the production run.

Trajectory analysis. The trajectories generated by Desmond were analyzed using the VMD 1.9.3 program.[45] The stability of the MD simulations was controlled through the energy, temperature, and root mean squared deviation (RMSD) profiles of the ribosome and the docked compounds. The RMSD profiles of the truncated ribosome and the compounds were calculated with respect to the initial structure based on all atoms of the nucleotides and the amino acids, as

$$\mathrm{RMSD}(v,w) = \sqrt{\frac{1}{n}\sum_{i=1}^{n}\left((v_{iz}-w_{iz})^2 + \left(v_{iy}-w_{iy}\right)^2 + (v_{ix}-w_{ix})^2\right)} \quad (2)$$

Hydrogen bonding and the other favorable non-bonded contacts and their occurrence percentages were calculated using the analyze_trajectory_ppi.py script in Maestro.

MM-GBSA binding free energy calculations. The binding free energies of the receptor-compound complexes were estimated using the one-trajectory approach[46] with the thermal_mmgbsa.py python script implemented in the Prime module of Schrödinger Suite (Schrödinger Release 2025-1) based on conformations obtained from the MD trajectories every 4 ns as follows,

$$\Delta G_{bind} = \Delta H - T\Delta S = \Delta E_{MM} + \Delta G_{sol} - T\Delta S \quad (3)$$

$$\Delta E_{MM} = \Delta E_{internal} + \Delta E_{elec} + \Delta E_{vDW} \quad (4)$$

$$\Delta G_{sol} = \Delta G_{GB} + \Delta G_{SA} \quad (5)$$

Here, the terms ΔE_{MM}, ΔG_{sol}, and $T\Delta S$ refer to the molecular mechanical energy, dissolution-free energy (the sum of polar ΔG_{GB} and nonpolar ΔG_{SA} contributions) and conformational entropy in the gas phase, respectively. The term ΔE_{MM} includes van der Waals energy (ΔE_{vDW}), electrostatic energy (ΔG_{elec}), and bond length, angle, and dihedral energies ($\Delta E_{internal}$). The entropy term $T\Delta S$ was neglected in the calculations, as similar types of compounds bind to the receptor, and the enthalpic contribution alone provides a sufficient basis for ranking different ligands.

In vitro assays

Drugs used. Clindamycin (DB01190), GSK-690693 (DB12745), Icatibant Acetate (DB06196), Mitoxantrone (DB01204), Piperaquine (DB13941), Setmelanotide (DB11700), Olcegepant (DB04869), and Vinorelbine (DB0036) were purchased from Selleckchem. Ciraparantag (DB15199) was purchased from TargetMol. Daunorubicin (DB00694), Elbasvir (DB11574), Plerixafor (DB06809), Tetrandrine (DB14066), Voacamine (DB04877), and Ziritaxestat (DB15403) were purchased from MedChemExpress. The drugs were stored as powders at −20 °C until use.

According to the manufacturers' data sheets, Ciraparantag, Daunorubicin, Icatibant Acetate, Mitoxantrone, Piperaquine, Plerixafor, Setmelanotide, and Vinorelbine were dissolved in water, while Clindamycin, Elbasvir, GSK-690693, Olcegepant, Tetrandrine, Voacamine, and Ziritaxestat were dissolved in DMSO. All prepared stock solutions were stored at −80 °C.

In preparation for the translational assay, drugs typically dissolved in DMSO were initially suspended in phosphate-buffered saline (PBS) due to the detected inhibitory effects of DMSO on luciferase-based translation assays. To aid in solubilization, HCl was added to the suspension, followed by neutralization with an equivalent amount of NaOH.

The minimum inhibitory concentration (MIC) and minimum bactericidal concentration (MBC) assays. The antibacterial potential of the drug candidates was evaluated by determining their MIC and MBC against *Escherichia coli* ATCC 10536 by using the broth microdilution method according to European Committee on Antimicrobial Susceptibility Testing (EUCAST) guidelines.[47] An overnight culture of *Escherichia coli* was inoculated into fresh Mueller–Hinton (MH) broth and incubated at 37 °C with shaking at 180 rpm until reaching an OD_{600} of 0.15–0.2 (10^8 CFU mL^{-1}). The culture was subsequently diluted 1 : 100 in MH broth to obtain a final inoculum of approximately 10^6 CFU mL^{-1} 50 μL of MH broth was dispensed into each well of a sterile microtiter plate. Drug stock solutions, initially prepared at a concentration of 512 μg mL^{-1}, were serially two-fold diluted in MH broth to achieve final concentrations ranging from 256 to 0.002 μg mL^{-1}. Thereafter, 50 μL of the diluted bacterial inoculum (~10^6 CFU mL^{-1}) was added to

each well, resulting in a final bacterial concentration of 1–5 × 10^5 CFU mL^{-1} per well. The plates were then mixed on an orbital shaker at room temperature for 30 min and then incubated at 37 °C without agitation for 20 h. Bacterial growth was evaluated by measuring OD_{600}, and MIC was defined as the lowest drug concentration that completely inhibited bacterial growth. For MBC determination, 100 μL aliquots from wells at or above the MIC were spread onto MH agar plates. After overnight incubation at 37 °C, the MBC was recorded as the lowest concentration yielding no visible colonies. Drug-free wells served as growth controls, Clindamycin was included as a positive control, 1% DMSO was used as a negative control, and bacterial-free wells were included as sterility controls. All assays were performed in triplicate.

Time-kill assays. Time-kill assays were conducted to determine the nature and extent of the antibacterial effect of the drug candidates against *Escherichia coli* ATCC 10536. A drug-free control was included to monitor the normal growth kinetics of bacteria in the absence of treatment. Experimental groups were treated with the test compounds at concentrations corresponding to MIC, 2× MIC, and 4× MIC concentrations in order to assess the dose-dependent effects on bacterial viability. At predetermined time intervals (0, 3, 6, 12, and 24 h), 100 μL samples were collected, serially diluted in sterile PBS, and plated on LB agar to determine viable cell counts. The assays were repeated at least two times. Bacterial viability was expressed as CFU mL^{-1}, and time-kill curves were generated by plotting $\log_{10}$-transformed CFU values against time. MBC was defined as the lowest drug concentration that achieved a 3 $\log_{10}$ (≥99.9%) reduction at any time point.

***In vitro* translation inhibition assay.** The inhibitory effects of drugs on bacterial protein synthesis were evaluated using the *Escherichia coli* S30 extract system for circular DNA (Promega, Cat. No. L1020). 10 μL of reaction mixtures containing 3 μL of S30 extract and 1 μL of either water or the drug solution were preincubated at 22 °C for 5 min. Translation was initiated by adding 6 μL of a master mix containing 1 μL of pBESTluc DNA (~0.4 μg), 1 μL of complete amino acid mixture, and 4 μL of S30 premix. The mixtures were vortexed, incubated at 37 °C for 60 minutes, and then placed on ice for 5 minutes to terminate the reaction. Luciferase expression was measured using the Dual-Glo® Luciferase Assay System (Promega, Cat. No. E2920). For this, 10 μL of each reaction was transferred to a 384-well flat-bottom white plate and mixed with 10 μL of Dual-Glo® Luciferase Reagent. After 10 min of incubation at room temperature (20–25 °C), luminescence was measured using a BioTek Synergy™ H1 microplate reader. Assays were independently repeated at least two times.

To assess potential luciferase inhibitors, drugs were also evaluated for their effects on luciferase enzyme activity. For this purpose, a reaction mixture was prepared by combining 1 μL of the drug solution or water as a control, 1 μL of QuantiLum® recombinant firefly luciferase (diluted $1:10^5$), and 8 μL of luciferase dilution reagent. Residual luciferase activity was then measured using the Dual-Glo® Luciferase Assay System (Promega).

Results and discussion

The crystal structure of the *E. coli* 50S large subunit in complex with lincosamide Clindamycin (PDB ID: 4v7v) was used for molecular docking calculations and molecular dynamics (MD) simulations. Clindamycin targets the PTC, where it interferes with the positioning of A-site tRNA during peptide bond formation.[36] To ensure the reliability of our computational pipeline, Clindamycin was first re-docked into its binding site using both Glide and AutoDock Vina. This validation step confirmed the ability of both programs to accurately reproduce the experimental binding pose. Subsequently, the interaction energy of Clindamycin was calculated using the Prime MM-GBSA approach to establish a benchmark for evaluating the compound libraries.

The docking scores and MM-GBSA values obtained for Clindamycin were utilized as threshold criteria to prioritize candidates from the virtual screening campaign. Hit compounds were further filtered by integrating these energetic metrics with the known interaction patterns of Clindamycin and the structural characteristics of established PTC-binding drugs. To refine the selection, a structure-based pharmacophore model was applied, ensuring that the identified ligands satisfied the essential spatial and chemical requirements for PTC inhibition. The stability of the predicted binding modes was then rigorously assessed through all-atom MD simulations in Desmond.[43] As a truncated ribosomal structure was used in the MD simulations, the structural integrity and non-bonded interactions in the binding site were first monitored for the Clindamycin complex, of which the interactions are well characterized. Finally, hit compounds with different chemical moieties were tested with *in vitro* assays as bacterial ribosome inhibitors. These validation calculations using Clindamycin were highly useful to fine-tune the parameters and models used throughout the calculations with the compound libraries, to filter the promising hit compounds at each calculation step, and to set a strong basis to ultimately determine inhibitor and lead compounds using *in vitro* assays. The computational workflow is summarized in Fig. 2.

Molecular docking calculations targeting the peptidyl transferase center

We first re-docked the native inhibitor Clindamycin into its native binding site (PDB ID: 4v7v)[36] as a validation step for Glide and AutoDock Vina before the molecular docking calculations using the virtual drug libraries. The scores for Clindamycin were determined as −9.29 kcal mol^{-1} (SP-docking in Glide), −11.02 kcal mol^{-1} (XP-docking in Glide) and −8.7 kcal mol^{-1} (AutoDock-Vina) for its re-docked poses with low root mean squared deviation (RMSD) values <0.4 Å from the crystal pose (Fig. S4–S6). These low RMSD values confirmed the accuracy of docking parameters for both programs. The interaction energy of Clindamycin with the binding site was calculated as −113.15 kcal mol^{-1} using the Prime MM-GBSA approach.

Molecular docking calculations were conducted for over 10 885 conformers of FDA-approved, experimental, and investigational drugs on the PTC region of *E. coli* 50S ribosome large subunit (PDB ID: 4v7v) using Maestro-Glide at standard

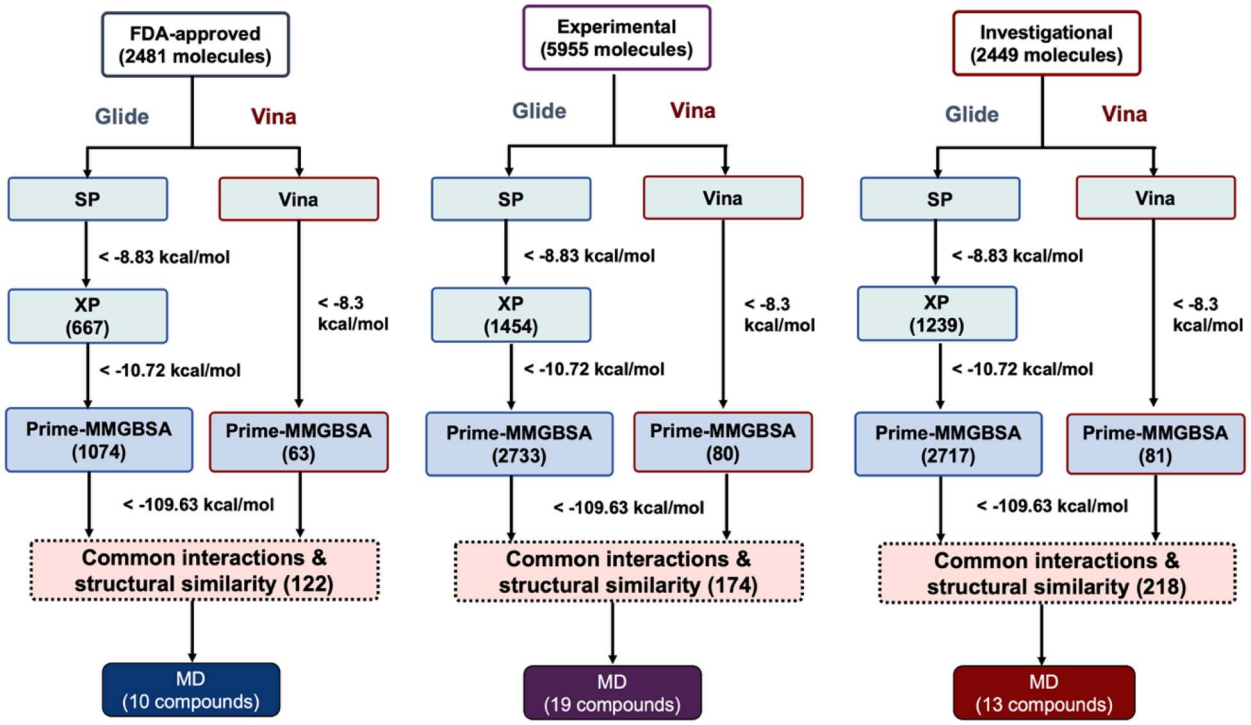

Fig. 2 Computational workflow for the identification of novel PTC inhibitors, which starts with a sequential filtering of FDA-approved, experimental, and investigational drug libraries using Glide (SP and XP modes) and AutoDock Vina. The number of compounds prioritized at each stage is indicated in parentheses. Threshold scores and binding energies (kcal mol^{-1}), established based on the benchmark inhibitor Clindamycin, are displayed alongside the corresponding filtering steps. The final selection for molecular dynamics (MD) simulations was based on consensus scoring, ligand-RNA interaction patterns common with known inhibitors, and structural similarity analysis for the compounds.

precision-SP and extra-precision-XP modes and AutoDock Vina (v.1.1.2) programs using the settings validated with Clindamycin calculations. During the docking calculations, the receptor was kept rigid, while the compounds were left flexible. Ligand poses produced as a result of SP-docking were sorted according to their GlideScore values. The compounds with scores better than -8.83 kcal mol^{-1}, which is 5% lower than SP-GlideScore of the crystal inhibitor Clindamycin, were sent to the next step, XP-docking to enhance the sampling (Fig. 2), as in our previous study.[34] In XP-docking results, the scores were ranked from best to worst, and compounds with an XP-GlideScore value (-10.72 kcal mol^{-1}) below 5% of that of Clindamycin were noted and included in Prime MM-GBSA calculations. For the AutoDock Vina results, the threshold value was taken as -8.3 kcal mol^{-1} to select the high-affinity compounds. The obtained compounds were then subjected to Prime MM-GBSA calculations and further filtered with a threshold value of 109.63 kcal mol^{-1}, which is 5% lower than the Prime MM-GBSA value of Clindamycin. This process yielded 122 compounds from the FDA-approved drug library, 174 compounds from the experimental drug library, and 218 compounds from the investigational drug library. Aminoglycoside group antibiotics, Apramycin, Dibekacin, Framycetin, Geneticin, Gentamicin, Kanamycin, Netilmicin, Ribostamycin, Streptomycin, and Tobramycin had the highest docking scores and Prime MM-GBSA values (not shown) but were not further investigated as they are known translation inhibitors.

To further filter the compounds with high affinity towards the PTC, a pharmacophore model was designed. With this aim, first, the 2-dimensional interaction diagrams of PTC-binding antibiotics from different families (A201A, Chloramphenicol, Hygromycin A, Clindamycin, Linezolid) were obtained from the crystal structures (Fig. S1). These antibiotics generally have hydrogen bond with the nucleotides A2058, A2059, G2061, A2062, G2505, A2503, U2506, G2583 and U2585, and π interactions (π-sigma, π–π interaction, π-sulfur) with the nucleotides A2451, C2452, U2504, G2505, and U2506 and halogen bond with nucleotide A2451 (Fig. S2 (a)), where G2505 is highlighted as the main target. In the pharmacophore model, 12 nucleotides (A2058, A2059, G2061, A2062, G2505, A2503, U2506, G2583, U2585, A2585, C2451, and U2504) were considered in the receptor cavity, and their features were selected to maximize binding (Fig. S2 (b)). The pharmacophore model contained a total of 8 features: hydrophobic (H18), aromatic ring (R24, R26, and R28), hydrogen bond acceptor (A1, A8), and hydrogen bond donor (D11, D12). The docked compounds that satisfied at least 5 out of the 8 features in the pharmacophore model were selected *via* phase screening.

After the pharmacophore design, the compounds having similar types of interactions as the PTC-binding antibiotics (Fig. S1 and S2) were considered. Accordingly, a total of 42 compounds (10 FDA-approved, 19 experimental, and 13 investigational compounds) were selected for further MD simulations. Fig. S7–S9 display the 2-dimensional interaction

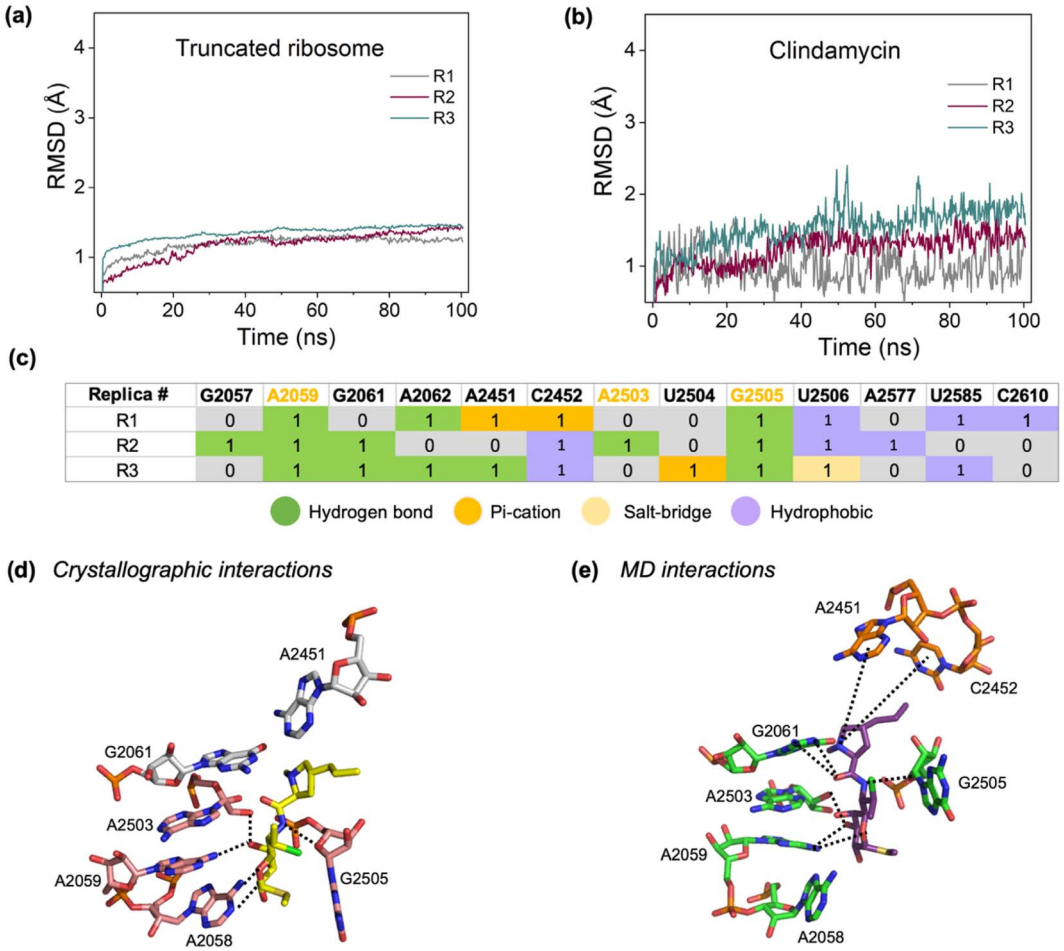

Replica #	G2057	A2059	G2061	A2062	A2451	C2452	A2503	U2504	G2505	U2506	A2577	U2585	C2610
R1	0	1	0	1	1	1	0	0	1	1	0	1	1
R2	1	1	1	0	0	1	1	0	1	1	1	0	0
R3	0	1	1	1	1	1	0	1	1	1	0	1	0

Fig. 3 RMSD profile of (a) the truncated ribosomal structure and (b) Clindamycin in three independent MD simulations. (c) Clindamycin interactions with 23S rRNA, which are observed in at least 10% of the trajectory in each replica, are displayed as a map. The nucleotides with known interactions with the antibiotic are highlighted in yellow at the top. The types of non-bonded interactions are color-coded as hydrogen bond (green), π-cation (orange), hydrophobic (slate), and salt-bridge (light orange). Involvement of the nucleotides in non-bonded interactions is indicated by 1, whereas their absence is indicated by 0. The critical interactions between Clindamycin and 23S rRNA are shown for (d) the crystal structure and (e) the MD simulations.

diagrams of the selected compounds from three drug libraries. These compounds make hydrogen-bond interactions with A2058, G2061, A2062, G2505, and U2506; π interactions with G2061, A2062, A2451, C2452, A2503, G2505, and U2585; and attractive charge interactions with G2505, similar to the PTC-binding antibiotics. The DrugBank ID, chemical structure, molecular weight, chemical class, SP-docking, XP-docking, AutoDock Vina, and Prime-MMGBSA scores of these compounds are listed in Tables S1–S3. It is also worth noting that the identified hits encompass diverse chemical scaffolds and therapeutic classes, including anticancer, antifungal, antiviral, and antimalarial agents, highlighting the potential for drug repurposing in the search for novel translation inhibitors.

Molecular dynamics simulations of the truncated ribosome in complex with Clindamycin

MD simulations of truncated ribosome-ligand complexes were performed to evaluate the stability of the docked compounds at their binding sites, analyze their interactions with nucleic acids and protein residues, and estimate the binding free energy of the compounds. As a truncated ribosomal structure was employed to maintain the computational efficiency, 3 × 100 ns long MD simulations of the Clindamycin-truncated ribosome complex from the crystal structure PDB ID: 4v7v were first carried out as a validation step. The experimentally known interactions of Clindamycin with the PTC served as a benchmark to demonstrate the accuracy of the simulation protocol. The structural stability and flexibility of the truncated ribosomal structure and Clindamycin were assessed by calculating RMSD values over all atoms, taking the initial frame of the production runs as the reference. RMSD values of the truncated ribosomal structure fluctuated around 1.0–1.2 Å during the simulations (Fig. 3(a)), which is expected since harmonic restraints were employed in the middle and outer regions to maintain the integrity of the truncated model throughout the simulations. Similarly, Clindamycin was stable in the binding site, with RMSD values fluctuating around 1.0–1.5 Å in all replicas (Fig. 3(b)).

Non-bonded interactions between Clindamycin and 23S rRNA were analyzed for each replica and given as a map in Fig. 3(c). Here, the interactions observed in at least 10% of the trajectories were considered. In all replicas, Clindamycin adopted a conformation similar to that observed in the *E. coli* ribosome-Clindamycin complex determined by crystallography,[36] aligning well with the drug's footprinting pattern (Fig. 3d and e). The antibiotic was noted to maintain its crystal contacts, especially with A2059 and G2505 through hydrogen bonding, and π-sulfur interactions with G2505. The drug made contact with A2058 in ∼9% of the trajectories in the form of hydrogen bonding. In the cavity, Clindamycin also interacted with G2061 and A2503 using hydrogen bonds, as well as A2451, C2452, and U2506 using π-cation and hydrophobic interactions. Previous footprinting data showed that Clindamycin protects A2058 and A2451 from dimethyl sulfate, G2505 and G2061 from kethoxal modification.[48] Modification at A2503 was shown to confer resistance to Clindamycin in *E. coli* and *S.* spp.[49] The findings for Clindamycin thus showed the reliability of the simulation protocol employed in this study. The binding free energy of Clindamycin was calculated using the MM-GBSA method[46] implemented in the Prime module of Schrödinger Suite (Schrödinger Release 2021-4). Its binding free energy varied between −27.47 kcal mol^{-1} and −31.85 kcal mol^{-1} in the MD simulations (Table S1).

Molecular dynamics simulations of the hit compounds docked to the peptidyl transferase center

After validating the MD protocol, the selected hit compounds (10 FDA-approved, 19 experimental, and 13 investigational compounds) were subjected to 3 × 100 ns long explicit MD simulations to monitor the extent of interactions with the binding site, and to calculate their binding free energy values. Fig. S10 displays the distribution of the RMSD values of the truncated ribosome and the docked FDA-approved drugs. RMSD of the truncated ribosome for all ligand-bound structures fluctuated around 1.0 Å (Fig. S10(a)). In general, the ligands maintained their docking poses in the binding site, except for Buserelin and Elbasvir in one replica, adjusting their flexible side chains (Fig. S10(b)). We further analyzed the non-bonded interactions between the docked compounds and the binding site observed in at least 10% of the MD trajectories, using the analyze_trajectory_ppi.py script implemented in Maestro (Fig. S11). This analysis showed which nucleotides and types of interactions were consistently observed to stabilize the compounds in the PTC. Notably, the docked compounds kept their interactions with one or more antibiotic-binding nucleotides in the PTC through favorable interactions. The binding energy values of the ligands were calculated for each replica using the MM-GBSA approach and presented in Table S1. The values were consistent for the replicas in the binding cavity. In addition, the binding poses of the experimental and investigational drugs in the PTC cavity were investigated with the RMSD profiles. The truncated ribosome was stable with narrow distributions with small RMSD values (Fig. S12(a) and S14(a)), and the compounds seemed to remain in the binding site (Fig. S12(b) and S14(b)), making favorable interactions with the same nucleotides (Fig. S13 and S15), where the types of interactions changed from one replica to another in some cases. The binding free energy values of the docked ligands were evaluated to rank the experimental (Table S2) and investigational hit compounds (Table S3).

The findings from the MD simulations confirmed the binding poses from the docking calculations. They also suggested that all investigated compounds had a high binding affinity to the target region, where the compounds made favorable interactions with the functional nucleotides. Therefore, they were selected as the superior candidates for further *in vitro* assays.

Based on the availability of the compounds, six FDA-approved compounds, namely Daunorubicin, Elbasvir, Mitoxantrone, Piperaquine, Plerixafor, and Vinorelbine, were evaluated in *in vitro* studies. In addition, two experimental drugs, DB014066 (Tetrandrine) and DB04877 (Voacamine); and three investigational drugs GSK-690693, Olcegepant and Ziritaxestat were tested. We also included two FDA-approved compounds in the *in vitro* assays, namely Icatibant, and Setmelanotide, and one investigational drug Ciraparantag, with high binding affinity to the decoding center from our previous study.[34]

Antibacterial efficacy of drug candidates

To validate the outcomes of the computational predictions, the antibacterial potential of the selected drug candidates (Icatibant Acetate, GSK-690693, Mitoxantrone, Piperaquine, Vinorelbine, Olcegepant, Ciraparantag, Tetrandrine, Voacamine, Daunorubicin, Elbasvir, Plerixafor, and Ziritaxestat) together with the reference compound of Clindamycin was initially assessed against *E. coli* ATCC 10536 using broth microdilution assays to determine their MIC and MBC values. Among these candidates, only Mitoxantrone and Daunorubicin exhibited antibacterial activity against *E. coli* ATCC 10536 (Table S4–S6). A notable activity was exhibited by Mitoxantrone with both MIC and MBC values of 64 μg mL^{-1}, while Daunorubicin showed the weakest activity, with MIC and MBC values of 128 μg mL^{-1} (Table 1 and Fig. S16–S18). The reference compound of Clindamycin showed a MIC value of 16 μg mL^{-1} and a MBC of 128 μg mL^{-1} against *E. coli* ATCC 10536, while the negative control containing 1% DMSO did not exhibit any inhibitory activity, thereby supporting the validity of the assay conditions used in this study.

Based on the notable antibacterial activity of Mitoxantrone, time-kill assays were performed at MIC, 2× MIC, 4× MIC over a 24 h period to investigate the nature and extent of its antibacterial effect. The results showed that Mitoxantrone exhibited a bacteriostatic effect against *E. coli* ATCC 10536 at MIC (64 μg mL^{-1}) and 2× MIC (128 μg mL^{-1}), whereas a bacteriocidal effect was observed at 4× MIC (256 μg mL^{-1}) (Fig. 4). These findings were also consistent with those reported for the reference drug Clindamycin, which is primarily known to exert a bacteriostatic effect against *E. coli* ATCC 105; however, at higher

Table 1 MIC and IC_{50} values of the drug candidates selected with *in silico* screening

Drug candidates	MIC[a] (μg ml^{-1})	IC_{50}[b] (μg ml^{-1})	IC_{50}[b] (μM)
Clindamycin	16.00	7.09 ± 0.16	16.55 ± 0.43
Ciraparantag	N/A	N/A	
Daunorubicin	128.00	N/A	
Elbasvir	N/A	N/A	
GSK-690693	N/A	N/A	
Icatibant acetate	N/A	N/A	
Mitoxantrone	64.00	7.30 ± 0.20	14.10 ± 0.38
Olcegepant	N/A	125.50 ± 14.27	144.30 ± 16.41
Piperaquine	N/A	N/A	
Plerixafor	N/A	31.62 ± 3.29	62.30 ± 6.47
Setmelanotide	N/A	N/A	
Tetrandrine	N/A	N/A	
Vinorelbine	N/A	N/A	
Voacamine	N/A	N/A	
Ziritaxestat	N/A	132.00 ± 14.72	224.30 ± 25.02

[a] N/A: no detectable antibacterial activity. [b] N/A: no detectable inhibitory activity.

concentrations, Clindamycin may also exhibit bactericidal activity,[50] similar to that observed for Mitoxantrone.

In vitro translation inhibition analysis

Gram-negative bacteria are intrinsically resistant to many antibiotics due to the permeability barrier formed by their outer membrane.[51,52] This could explain why almost all candidate compounds, except Mitoxantrone and Daunorubicin, failed to exhibit antibacterial activity against *E. coli* in the microdilution assay. To rule out this possibility, all candidate compounds were subsequently screened for their potential to inhibit translation in *E. coli* using a luciferase-based *in vitro* protein synthesis assay. Mitoxantrone and Daunorubicin were tested at their respective MIC concentrations, while other drug candidates, along with Ampicillin (used as a negative control), were evaluated at a final concentration of 100 μg mL^{-1}, which was the maximum concentration permissible under our assay conditions. Initial screening revealed that Clindamycin (reference drug, positive control), Mitoxantrone, Daunorubicin, Plerixafor, Olcegepant, and Ziritaxestat have the ability to inhibit protein synthesis. These compounds were then assessed for potential direct interference with luciferase enzyme activity. None of them exhibited any inhibitory effect on the luciferase enzyme, confirming that the observed reduction in signal was due to translation inhibition rather than enzyme inhibition. Therefore, all six compounds were deemed suitable for further testing to determine their IC_{50} values for *E. coli* translation inhibition. To this end, bacterial translation inhibition assays were conducted by measuring changes in luciferase expression across increasing drug concentrations (Fig. 5). Due to its intense red pigmentation, Daunorubicin produced inconsistent and non-reproducible results across independent experiments, which prevented the accurate determination of its IC_{50} value. This variability is likely caused by optical interference: the bioluminescence generated by firefly luciferase (FLuc), which emits light in the 500–600 nm range, can be attenuated by highly pigmented compounds such as red, blue, or black dyes. Signal suppression is particularly pronounced at compound concentrations above 10 μM and depends on the absorbance properties of the compound at the detection wavelength.[53] IC_{50} values for the remaining compounds were reliably determined (Table 1). Among these, the most potent drug was Mitoxantrone, which exhibited an IC_{50} of 7.30 ± 0.20 μg mL^{-1} or 14.10 ± 0.38 μM, comparable to that of Clindamycin (7.09 ± 0.16 μg mL^{-1} or 16.55 ± 0.43 μM), suggesting similar affinities for the target ribosome (Fig. 5). This result positions Mitoxantrone as a promising candidate for ribosome-targeted antibacterial development. It is noteworthy that while the IC_{50} values of these compounds were comparable, their MIC values differed by a factor of four, suggesting that differences in outer membrane permeability may influence their antibacterial efficacy. This observation aligns with previous findings that the outer membrane of Gram-negative bacteria can act as a significant barrier to many antimicrobial agents, thereby reducing their effective intracellular concentrations.[51]

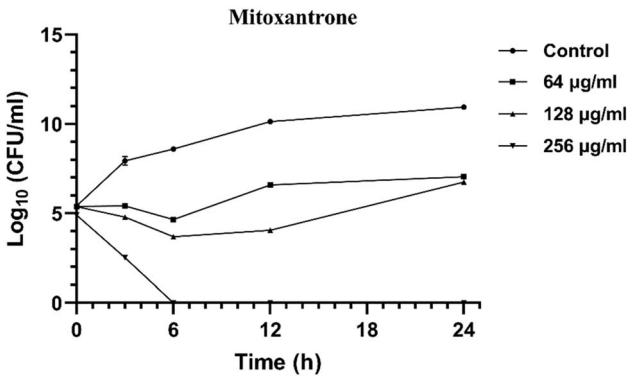

Fig. 4 Time-kill curve of Mitoxantrone. Error bars represent standard error of the mean. Any error bars that are not visible are smaller than the data symbols.

In contrast to Mitoxantrone, Plerixafor (IC_{50} 31.62 ± 3.29 μg mL^{-1}), Olcegepant (IC_{50} 125.5 ± 14.27 μg mL^{-1}), and Ziritaxestat (IC_{50} 132 ± 14.72 μg mL^{-1}) showed markedly higher IC_{50} values, indicating substantially weaker translation inhibition (Fig. 5). Although these compounds may bind to the ribosome, their rapid dissociation could preclude effective translational suppression. This suggests that compounds predicted *in silico* to form stable ribosome complexes may instead dissociate rapidly under experimental conditions, thereby reducing their inhibitory potency. Moreover, although these drug candidates inhibited translation *in vitro*, they failed to exhibit antibacterial activity against *E. coli*, strongly suggesting the presence of a cell-entry barrier limiting their intracellular access. Most likely, these compounds may be unable to efficiently penetrate the outer membrane of *E. coli*, thereby limiting their antibacterial efficacy.

Binding modes of the identified translation inhibitors

In vitro translation inhibition assays identified one inhibitor, namely Mitoxantrone, and three lead compounds, Plerixafor,

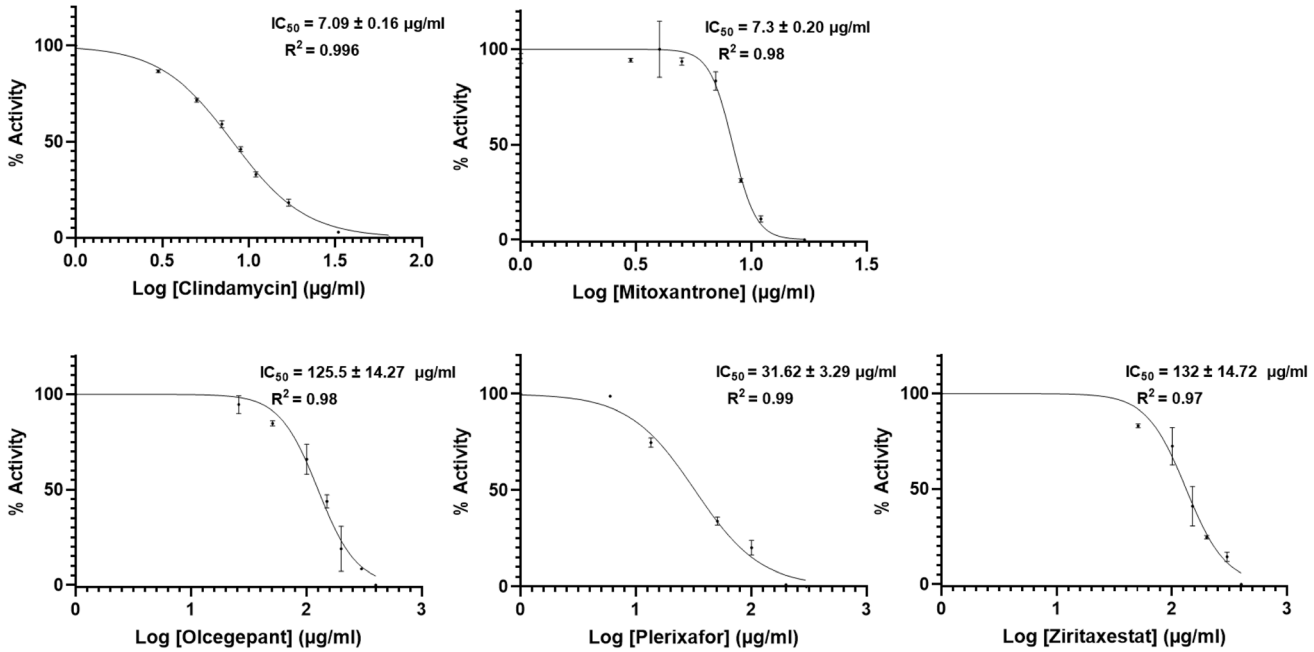

Fig. 5 *In vitro* inhibition of protein synthesis by Clindamycin (control) and the drug candidates in the *E. coli* cell-free translation system. Error bars represent standard error of the mean. Any error bars that are not visible are smaller than the data symbols.

Olcegepant, and Ziritaxestat, targeting *E. coli* ribosome and inhibiting protein synthesis. The antibacterial effect of Mitoxantrone was previously reported for Gram-positive bacteria.[54] To further elucidate their potential as novel rRNA-targeting therapeutics, we conducted a detailed analysis of the non-bonded interactions between the compounds and the catalytic cavity, with a particular focus on critical nucleotides conferring resistance to antibiotics. An antibiotic fingerprint was constructed based on structural data from known PTC-targeting antibiotics. The fingerprint revealed the nucleotides associated with the binding of antibiotics: Clindamycin (A2058, A2059, A2503, and G2505),[36] Chloramphenicol (A2062 and G2505),[36] Linezolid (A2062, U2504, and G2505),[55] Hygromycin A (G2061, A2062, A2503, G2505, U2506, and U2585),[56] and A201A (A2059, G2061, A2062, A2503, G2505, and G2583)[56] (Fig. 6).

The fingerprint given in Fig. 6 indicates the interactions of identified compounds with the PTC cavity that occurred in at least 10% of the production runs and were present in at least two out of the three replicas. Mitoxantrone formed stable interactions with A2503, U2504, G2505 and C2610 *via* its flexible chains, accommodating multiple NH and OH groups. In addition, its fused ring interacted with G2061 and A2062 (Fig. 6, and S19). Indeed, Mitoxantrone was shown to have high binding affinity for RNA that was validated with a computational and experimental study.[24] Plerixafor, a bicyclam chemokine receptor CXCR4 antagonist (also known as AMD-3100),[57] was stable in the binding cavity with RMSD around 1.7 Å in all replicas (Fig. S20). One of the bicyclams in its structure formed hydrogen bond and salt bridge interactions with U2441 and C2442, respectively. Olcegepant, the first calcitonin gene-related peptide (CGRP) receptor antagonist for migraine treatment,[58] and anticancer drug Ziritaxestat, both contain a piperazine fragment. Olcegepant maintained its docking pose mostly *via* hydrogen bond interactions with G2061, A2062, G2505, U2506 and π–π interactions with A2503, U2504, and U2586 (Fig. S21). Ziritaxestat generally remained stable in the initial docking site, maintaining π–π interactions with A2062 and G2505 (Fig. S22).

These four compounds were stabilized by the nucleotides whose modification or mutation confer resistance to antibiotics in various organisms. Mutations in nucleotides A2058 and A2059 conferred resistance to lincosamides[33,48,59,60] as well as oxazolidinones in *M. smegmatis*,[61] and macrolides in *S. pyogenes*, and *T. otitidis*.[62–69] It is worth mentioning that Mitoxantrone was not noted to interact with A2058 and A2059. On the other hand, the G2061A mutant has been reported to have a sensitivity to macrolides, but not to Tiamulin, Lincomycin, or Chloramphenicol in *T. thermophilus*.[70] Single-point mutations at A2062 nucleotide did not notably affect sensitivity of the *E. coli* cells to Erythromycin binding to the nascent polypeptide exit tunnel entrance[71] but conferred resistance to Chloramphenicol in *H. halobium*.[72] Methylation at A2503 causes resistance to Chloramphenicol, Florfenicol and Clindamycin in *Staphylococcus* spp. and *E. coli*.[73] Mitoxantrone and Olcegepant interacted with U2504, where the lack of pseudouridines at this nucleotide significantly affects *E. coli* growth and confers resistance to peptidyl transferase inhibitors.[74,75] The antibiotic resistance due to the mutation or modification of this nucleotide is also noted in other species.[72] Moreover, mutations at the neighboring nucleotides can also confer resistance to antibiotics by changing the positioning of U2504.[76] Single-point mutation studies on positions 2058, 2503 and 2504, either alone or in combination with other mutations, have been shown to confer resistance to lincosamides, oxazolidinones, and macrolides in *M. smegmatis*.[61,77] A moderate, 8-fold increase

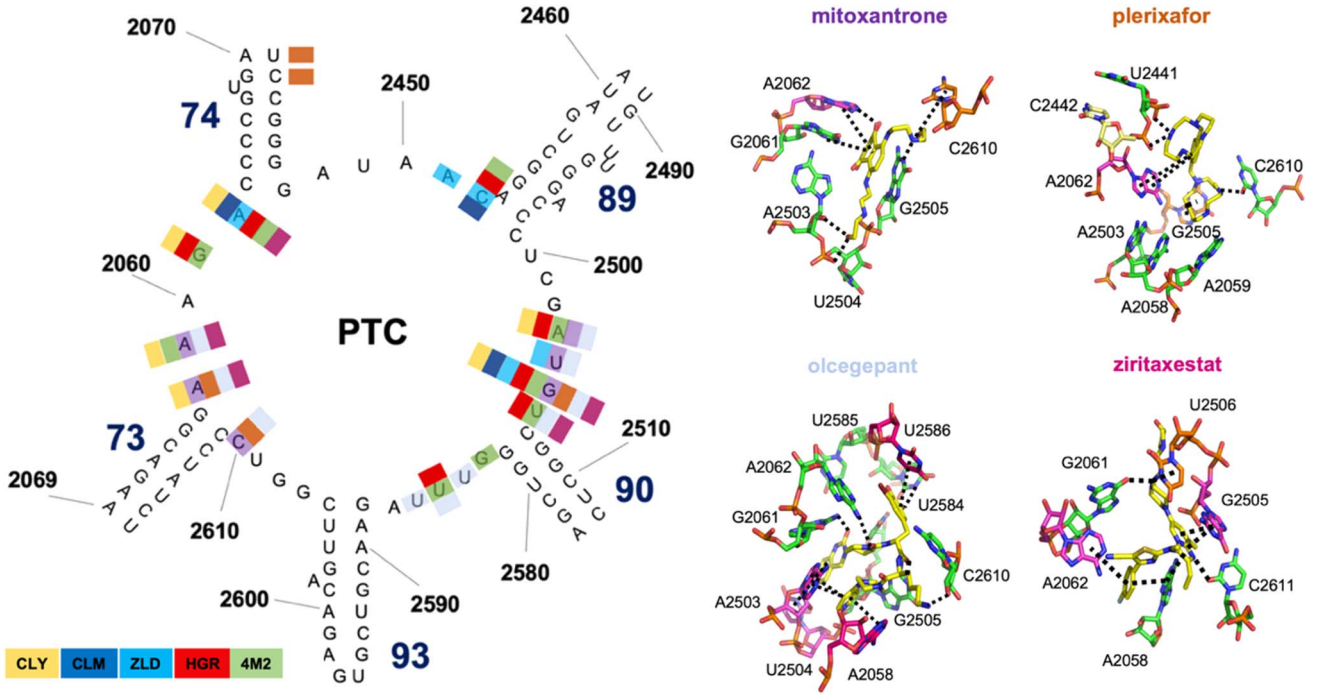

Fig. 6 23S rRNA-ligand interaction fingerprint based on Clindamycin (CLY, in yellow), Chloramphenicol (CLM, in blue), Linezolid (ZLD, in cyan), Hygromycin A (HGR, in red) and A201A (4M2, in green) binding sites is shown on the 23S rRNA secondary structure. The inhibitor Mitoxantrone (purple), the lead compounds Plerixafor (orange), Olcegepant (slate), and Ziritaxestat (pink), and their favorable interactions (hydrogen bond, π–cation, π–π, salt-bridges) are also indicated on the secondary structure (on the left panel) and the three-dimensional structures (on the right panel).

in linezolid minimum inhibitory concentrations was observed in the G2505A mutants in *M. smegmatis*; however, no resistance to Clindamycin was detected.[77] On the other hand, Mitoxantrone, Plerixafor and Olcegepant were stabilized by C2610, where C2610U substitution did not lead to a notable resistance.[78] Single-point mutation on C2611 in the *E. coli* ribosome confers resistance to Erythromycin binding to the entrance of the exit tunnel.[79] As noted, the modifications and mutations of antibiotic-binding nucleotides can have different effects on the protein translation from one organism to another. Therefore, the *E. coli* translation inhibitor Mitoxantrone and the three lead compounds should be further evaluated against antibiotic-resistant *E. coli* strains. Consequently, the identification of Mitoxantrone as *E. coli* translation inhibitor, alongside the three identified lead compounds, provides a compelling framework for the development of next-generation therapeutics.

Conclusion

In this study, we followed a comprehensive computational pipeline to identify hit compounds targeting the peptidyl transferase center (PTC) of the bacterial ribosome among FDA-approved, investigational, and experimental compounds, which were suggested for the *in vitro* assays. Both microdilution and inhibition translation assays identified Mitoxantrone as an inhibitor with IC_{50} of 14.10 ± 0.38 μM, comparable to the antibiotic Clindamycin (16.55 ± 0.43 μM). On the other hand, inhibition translation assays also determined three lead compounds, Plerixafor (IC_{50} = 62.30 ± 6.47 μM), Olcegepant (IC_{50} = 144.30 ± 16.41 μM), and Ziritaxestat (IC_{50} = 224.30 ± 25.02 μM), showing inhibitory effects on the ribosome of *E. coli* strain. While the lead compounds are highly promising to treat infections due to Gram-negative bacteria after modifications necessary to pass the outer membrane, the anti-cancer agent Mitoxantrone seems to be a dual-action therapeutic,[80] to simultaneously combat cancer and bacterial infections, which is highly important to increase cancer patients' quality of life. Mitoxantrone is not a clinically applicable antibacterial agent in its current form. Any future consideration in this direction would require substantial optimization to overcome its known toxicity and pharmacokinetic/pharmacological limitations. It is worth noting that the identification of Mitoxantrone as an FDA-approved ribosome inhibitor and the lead compounds enables a repurposing strategy and offers a well-defined scaffold for optimization, with future work focusing on using a high-resolution imaging technique to confirm precise binding sites of these compounds on the bacterial ribosome.

This successful result was achieved through the utilization of molecular docking and molecular dynamics (MD) simulations, along with filtering procedures carefully employed to increase the number of true positives. In addition, two docking tools, Glide and AutoDock Vina, with different scoring functions were used for consensus docking. Another important step in the computational protocol was the validation of rRNA docking and MD simulations; the settings for both docking programs and

the default relaxation protocol of Desmond were carefully fine-tuned by examining the interactions of the native inhibitor Clindamycin with the PTC cavity. This study also demonstrated that the usage of a truncated ribosome structure in the 100 ns long MD simulations with multiple replicas was able to show the extent of interactions between the docked compounds and the rRNA.

To the best of our knowledge, this is the first study used to repurpose drugs for the PTC region by employing such a hierarchical virtual screening method confirmed by *in vitro* assays. Therefore, the detailed protocols explained in this study offer a promising recipe for identifying effective modulators to target many challenging systems, including supramolecular structures and RNA complexes, to help the RNA research in medicinal chemistry.

Author contributions

MY: writing – original draft, investigation, methodology, validation, formal analysis, visualization. E. K.: writing – original draft, investigation, methodology, validation, formal analysis. F. A. S.: writing – review & editing, validation, supervision, conceptualization. A. K.: writing – review & editing, validation, supervision, conceptualization. O. K.: writing – review & editing, visualization, supervision, methodology, project administration, resources, funding acquisition, conceptualization.

Conflicts of interest

The authors declare that they have no known competing financial interests or personal relationships that could have appeared to influence the work reported in this article.

Data availability

The data supporting this article have been included as part of the supplementary information (SI). Supplementary information is available. See DOI: https://doi.org/10.1039/d6ra01785a.

Acknowledgements

This work was supported by the Scientific and Technological Research Council of Turkey (TÜBİTAK) under project number 121Z330 (Program 1001) and the Istanbul Technical University Scientific Research Projects Coordination Unit (ITU-BAP) through General Research Project TGA-2023-44708. MY and OK acknowledge the support of ITU-BAP project MDK-2023-44615. EK and AK acknowledge the support of ITU-BAP Project TDK-2022-44130. The authors acknowledge the National Center for High Performance Computing of Turkey (UHeM) at ITU for providing the computing resources under grant number 5013702022. MY also acknowledges the TÜBİTAK 2211/C National PhD Scholarship Program in the Priority Fields in Science and Technology for financial support.

References

1 Md. A. Salam, Md. Y. Al-Amin, M. T. Salam, J. S. Pawar, N. Akhter, A. A. Rabaan and M. A. A. Alqumber, *Healthcare*, 2023, **11**, 1946.
2 L. Zhang, J. He, L. Bai, S. Ruan, T. Yang and Y. Luo, *Med. Res. Rev.*, 2021, **41**, 1855–1889.
3 J. Lin, D. Zhou, T. A. Steitz, Y. S. Polikanov and M. G. Gagnon, *Annu. Rev. Biochem.*, 2018, **87**, 451–478.
4 J. Poehlsgaard and S. Douthwaite, *Nat. Rev. Microbiol.*, 2005, **3**, 870–881.
5 K. J. Y. Wu, B. I. C. Tresco, A. Ramkissoon, E. V. Aleksandrova, E. A. Syroegin, D. N. Y. See, P. Liow, G. A. Dittemore, M. Yu, G. Testolin, M. J. Mitcheltree, R. Y. Liu, M. S. Svetlov, Y. S. Polikanov and A. G. Myers, *Science*, 2024, **383**, 721–726.
6 S. M. Lauer, M. Reepmeyer, O. Berendes, D. Klepacki, J. Gasse, S. Gabrielli, H. Grubmüller, L. V. Bock, A. Krizsan, R. Nikolay, C. M. T. Spahn and R. Hoffmann, *Nat. Commun.*, 2024, **15**, 3945.
7 C.-X. Ma, Y. Li, W.-T. Liu, Y. Li, F. Zhao, X.-T. Lian, J. Ding, S.-M. Liu, X.-P. Liu, B.-Z. Fan, L.-Y. Liu, F. Xue, J. Li, J.-R. Zhang, Z. Xue, X.-T. Pei, J.-Z. Lin and J.-H. Liang, *Cell Discov.*, 2024, **10**, 75.
8 B. I. C. Tresco, K. J. Y. Wu, A. Ramkissoon, E. V. Aleksandrova, M. Purdy, D. N. Y. See, R. Y. Liu, Y. S. Polikanov and A. G. Myers, *Nat. Chem.*, 2025, **17**, 582–589.
9 H. Zhu, Y. Zhang, W. Li and N. Huang, *Int. J. Mol. Sci.*, 2022, **23**, 15961.
10 S. Pushpakom, F. Iorio, P. A. Eyers, K. J. Escott, S. Hopper, A. Wells, A. Doig, T. Guilliams, J. Latimer, C. McNamee, A. Norris, P. Sanseau, D. Cavalla and M. Pirmohamed, *Nat. Rev. Drug Discov.*, 2019, **18**, 41–58.
11 Y. Zhou, Y. Jiang and S. Chen, *WIREs Comput. Mol. Sci.*, 2022, **12**, e1571.
12 J. Manigrasso, M. Marcia and M. De Vivo, *Chem*, 2021, **7**, 2965–2988.
13 F. Barbault, B. Ren, J. Rebehmed, C. Teixeira, Y. Luo, O. Smila-Castro, F. Maurel, B. Fan, L. Zhang and L. Zhang, *Eur. J. Med. Chem.*, 2008, **43**, 1648–1656.
14 P. Daldrop, F. E. Reyes, D. A. Robinson, C. M. Hammond, D. M. Lilley, R. T. Batey and R. Brenk, *Chem. Biol.*, 2011, **18**, 324–335.
15 Y. Li, J. Shen, X. Sun, W. Li, G. Liu and Y. Tang, *J. Chem. Inf. Model.*, 2010, **50**, 1134–1146.
16 P. Pfeffer and H. Gohlke, *J. Chem. Inf. Model.*, 2007, **47**, 1868–1876.
17 A. Philips, K. Milanowska, G. Łach and J. M. Bujnicki, *RNA*, 2013, **19**, 1605–1616.
18 S. Chhabra, J. Xie and A. T. Frank, *J. Phys. Chem. B*, 2020, **124**, 4436–4445.
19 F. Stefaniak and J. M. Bujnicki, *PLoS Comput. Biol.*, 2021, **17**, e1008309.
20 S. Ruiz-Carmona, D. Alvarez-Garcia, N. Foloppe, A. B. Garmendia-Doval, S. Juhos, P. Schmidtke, X. Barril,

R. E. Hubbard and S. D. Morley, *PLoS Comput. Biol.*, 2014, **10**, e1003571.
21 A. A. Kognole, A. Hazel and A. D. MacKerell, *J. Chem. Theory Comput.*, 2022, **18**, 5672–5691.
22 F. P. Panei, P. Gkeka and M. Bonomi, *Nat. Commun.*, 2024, **15**, 5725.
23 N. A. Szulc, Z. Mackiewicz, J. M. Bujnicki and F. Stefaniak, *Briefings Bioinf.*, 2023, **24**, bbad187.
24 S. Sun and L. Gao, *Bioinformatics*, 2024, **40**, btae155.
25 J. G. Carvajal-Patiño, V. Mallet, D. Becerra, L. F. Niño Vasquez, C. Oliver and J. Waldispühl, *Nat. Commun.*, 2025, **16**, 2799.
26 M. R. Tirumalai, M. Rivas, Q. Tran and G. E. Fox, *Microbiol. Mol. Biol. Rev.*, 2021, **85**, e00104–e00121.
27 D. N. Wilson, *Nat. Rev. Microbiol.*, 2014, **12**, 35–48.
28 R. A. Friesner, J. L. Banks, R. B. Murphy, T. A. Halgren, J. J. Klicic, D. T. Mainz, M. P. Repasky, E. H. Knoll, M. Shelley, J. K. Perry, D. E. Shaw, P. Francis and P. S. Shenkin, *J. Med. Chem.*, 2004, **47**, 1739–1749.
29 O. Trott and A. J. Olson, *J. Comput. Chem.*, 2010, **31**, 455–461.
30 K. Palacio-Rodríguez, I. Lans, C. N. Cavasotto and P. Cossio, *Sci. Rep.*, 2019, **9**, 5142.
31 H. L. Nguyen, D. L. Pham, E. P. O'Brien and M. S. Li, *Sci. Rep.*, 2018, **8**, 6460.
32 H. L. Nguyen, P. H. An, N. Q. Thai, H. Q. Linh and M. S. Li, *J. Mol. Graph. Model.*, 2019, **91**, 80–90.
33 K. Kulczycka-Mierzejewska, J. Sadlej and J. Trylska, *J. Mol. Model.*, 2018, **24**, 191.
34 M. Yuce, B. Ates, N. I. Yasar, F. A. Sungur and O. Kurkcuoglu, *J. Mol. Graph. Model.*, 2024, **131**, 108817.
35 G. A. Kaminski, R. A. Friesner, J. Tirado-Rives and W. L. Jorgensen, *J. Phys. Chem. B*, 2001, **105**, 6474–6487.
36 J. A. Dunkle, L. Xiong, A. S. Mankin and J. H. D. Cate, *Proc. Natl. Acad. Sci. U. S. A*, 2010, **107**, 17152–17157.
37 G. Madhavi Sastry, M. Adzhigirey, T. Day, R. Annabhimoju and W. Sherman, *J. Comput. Aided Mol. Des.*, 2013, **27**, 221–234.
38 R. A. Friesner, R. B. Murphy, M. P. Repasky, L. L. Frye, J. R. Greenwood, T. A. Halgren, P. C. Sanschagrin and D. T. Mainz, *J. Med. Chem.*, 2006, **49**, 6177–6196.
39 J. L. Banks, H. S. Beard, Y. Cao, A. E. Cho, W. Damm, R. Farid, A. K. Felts, T. A. Halgren, D. T. Mainz, J. R. Maple, R. Murphy, D. M. Philipp, M. P. Repasky, L. Y. Zhang, B. J. Berne, R. A. Friesner, E. Gallicchio and R. M. Levy, *J. Comput. Chem.*, 2005, **26**, 1752–1780.
40 D. Devaurs, D. A. Antunes, S. Hall-Swan, N. Mitchell, M. Moll, G. Lizée and L. E. Kavraki, *BMC Mol. Cell Biol.*, 2019, **20**, 42.
41 J. Li, R. Abel, K. Zhu, Y. Cao, S. Zhao and R. A. Friesner, *Proteins*, 2011, **79**, 2794–2812.
42 M. C. Small, P. Lopes, R. B. Andrade and A. D. MacKerell, *PLoS Comput. Biol.*, 2013, **9**, e1003113.
43 K. J. Bowers, D. E. Chow, H. Xu, R. O. Dror, M. P. Eastwood, B. A. Gregersen, J. L. Klepeis, I. Kolossvary, M. A. Moraes, F. D. Sacerdoti, J. K. Salmon, Y. Shan and D. E. Shaw, in *ACM/IEEE SC 2006 Conference (SC'06)*, Tampa, FL, IEEE, 2006, pp. 43.
44 U. Essmann, L. Perera, M. L. Berkowitz, T. Darden, H. Lee and L. G. Pedersen, *J. Chem. Phys.*, 1995, **103**, 8577–8593.
45 W. Humphrey, A. Dalke and K. Schulten, *J. Mol. Graph.*, 1996, **14**, 33–38.
46 N. Homeyer and H. Gohlke, *Mol. Inf.*, 2012, **31**, 114–122.
47 European Committee for Antimicrobial Susceptibility Testing (EUKAST) of the European Society of Clinical Microbiology and Infectious Diseases, *Clin. Microbiol. Infect.*, 2003, **9**, ix–xv.
48 S. Douthwaite, *Nucleic Acids Res.*, 1992, **20**, 4717–4720.
49 C. Kehrenberg, S. Schwarz, L. Jacobsen, L. H. Hansen and B. Vester, *Mol. Microbiol.*, 2005, **57**, 1064–1073.
50 J. Spížek and T. Řezanka, *Appl. Microbiol. Biotechnol.*, 2004, **64**, 455–464.
51 A. H. Delcour, *Biochim. Biophys. Acta, Proteins Proteomics*, 2009, **1794**, 808–816.
52 C. Maher and K. A. Hassan, *mBio*, 2023, **14**, e0120523.
53 D. S. Auld and J. Inglese, in *Assay Guidance Manual*, Eli Lilly & Company and the National Center for Advancing Translational Sciences, Bethesda (MD), 2018.
54 R. A. G. Da Silva, J. J. Wong, H. Antypas, P. Y. Choo, K. Goh, S. Jolly, C. Liang, L. Tay Kwan Sing, M. Veleba, G. Hu, J. Chen and K. A. Kline, *Sci. Adv.*, 2023, **9**, eadd9280.
55 K. Tsai, V. Stojković, D. J. Lee, I. D. Young, T. Szal, D. Klepacki, N. Vázquez-Laslop, A. S. Mankin, J. S. Fraser and D. G. Fujimori, *Nat. Struct. Mol. Biol.*, 2022, **29**, 162–171.
56 Y. S. Polikanov, A. L. Starosta, M. F. Juette, R. B. Altman, D. S. Terry, W. Lu, B. J. Burnett, G. Dinos, K. A. Reynolds, S. C. Blanchard, T. A. Steitz and D. N. Wilson, *Mol. Cell*, 2015, **58**, 832–844.
57 C. W. Hendrix, C. Flexner, R. T. MacFarland, C. Giandomenico, E. J. Fuchs, E. Redpath, G. Bridger and G. W. Henson, *Antimicrob. Agents Chemother.*, 2000, **44**, 1667–1673.
58 S. J. Tepper, *Headache*, 2018, **58**, 238–275.
59 J. Poehlsgaard, P. Pfister, E. C. Böttger and S. Douthwaite, *Antimicrob. Agents Chemother.*, 2005, **49**, 1553–1555.
60 M. C. Roberts and J. Sutcliffe, in *Frontiers in Antimicrobial Resistance: a Tribute to Stuart B. Levy*, ASM Press, Washington, DC, USA, 2005.
61 B.-B. Li, C.-M. Wu, Y. Wang and J.-Z. Shen, *J. Antimicrob. Chemother.*, 2011, **66**, 1983–1986.
62 R. Leclercq, *Clin. Infect. Dis.*, 2002, **34**, 482–492.
63 C. D. Sigmund, M. Ettayebi and E. A. Morgan, *Nucleic Acids Res.*, 1984, **12**, 4653–4664.
64 A. S. Bommakanti, L. Lindahl and J. M. Zengel, *RNA*, 2008, **14**, 460–464.
65 C. Fyfe, T. H. Grossman, K. Kerstein and J. Sutcliffe, *Cold Spring Harb. Perspect. Med.*, 2016, **6**, a025395.
66 B. Vester and S. Douthwaite, *Antimicrob. Agents Chemother.*, 2001, **45**, 1–12.
67 S. Douthwaite, *J. Bacteriol.*, 1992, **174**, 1333–1338.
68 J. Jalava, M. Vaara and P. Huovinen, *Ann. Clin. Microbiol. Antimicrob.*, 2004, **3**, 5.
69 L. Boumghar-Bourtchai, H. Chardon, B. Malbruny, S. Mezghani, R. Leclercq and A. Dhalluin, *Int. J. Antimicrob. Agents*, 2009, **34**, 274–277.

70 E. E. Killeavy, G. Jogl and S. T. Gregory, *Antibiotics*, 2020, **9**, 313.
71 N. Vazquez-Laslop, C. Thum and A. S. Mankin, *Mol. Cell*, 2008, **30**, 190–202.
72 P. Kloss, L. Xiong, D. L. Shinabarger and A. S. Mankin, *J. Mol. Biol.*, 1999, **294**, 93–101.
73 C. Kehrenberg, S. Schwarz, L. Jacobsen, L. H. Hansen and B. Vester, *Mol. Microbiol.*, 2005, **57**, 1064–1073.
74 S.-M. Toh and A. S. Mankin, *J. Mol. Biol.*, 2008, **380**, 593–597.
75 C. Persaud, Y. Lu, A. Vila-Sanjurjo, J. L. Campbell, J. Finley and M. O'Connor, *Biochem. Biophys. Res. Commun.*, 2010, **392**, 223–227.
76 D. N. Wilson, F. Schluenzen, J. M. Harms, A. L. Starosta, S. R. Connell and P. Fucini, *Proc. Natl. Acad. Sci. U. S. A*, 2008, **105**, 13339–13344.
77 K. S. Long, C. Munck, T. M. B. Andersen, M. A. Schaub, S. N. Hobbie, E. C. Böttger and B. Vester, *Antimicrob. Agents Chemother.*, 2010, **54**, 4705–4713.
78 A. Canu, B. Malbruny, M. Coquemont, T. A. Davies, P. C. Appelbaum and R. Leclercq, *Antimicrob. Agents Chemother.*, 2002, **46**, 125–131.
79 P. Vannuffel, M. Di Giambattista, E. A. Morgan and C. Cocito, *J. Biol. Chem.*, 1992, **267**, 8377–8382.
80 A. Upadhyay, H. Chandra Jha, D. Pal and A. Kumar, *Cancer Pathog. Ther.*, 2025, **3**, 473–483.